

# NEUTRON, X-RAY, AND FINITE-ELEMENT STRESS ANALYSIS ON BRAZED COMPONENTS OF STEEL AND CEMENTED CARBIDE

L. PINTSCHOVIOUS<sup>a,b,\*</sup>, B. SCHREIECK<sup>c</sup>  
and B. EIGENMANN<sup>c</sup>

<sup>a</sup>*Forschungszentrum Karlsruhe, INFP, P.O. Box 3640,  
D-76021 Karlsruhe, Germany;* <sup>b</sup>*Laboratoire Léon Brillouin,  
C.E.-Saclay, F-91191 Gif-sur-Yvette Cedex, France;* <sup>c</sup>*Universität Karlsruhe  
(TH), Institut für Werkstoffkunde I P.O. Box 6980,  
D-76128 Karlsruhe, Germany*

Plates of cemented carbide were joined to steel by brazing. The structure was designed in imitation of a rock drill. Two types of steel were used which, after cooling from brazing temperature, showed a normalized ferritic–perlite or a martensitic material state, respectively. Copper foil containing a nickel mesh was used as braze material. The residual stresses resulting from the different thermal shrinkage and elastic–plastic behavior of the materials as well as from the different phase transformation behavior of the steels during cooling of the samples from the brazing temperature (1100°C) to room temperature were investigated by neutron diffraction with special attention to the regions near the interface between steel and cemented carbide. Additional measurements were performed by X-ray diffraction on selected surface areas. Most of the experimental results could be satisfactorily modelled by three-dimensional finite-element calculations employing the temperature dependent elastic–plastic behavior of the materials. In particular, characteristic differences between the residual stress states of components with ferritic–perlite or martensitic steel bodies were found experimentally as well as by the model calculations. Some points are discussed which require further investigations.

**Keywords:** Residual stresses; Brazed joints; Finite element calculations; Neutron stress analysis; X-ray stress analysis

---

\* Corresponding author.

## INTRODUCTION

Cemented carbides, in particular WC-based sintered alloys, are widely used for cutting tools. Because of their brittleness, the cemented carbides are usually joined with steel bodies. One well established method for joining cemented carbides with steel is brazing which, however, leads to considerable residual stresses after cooling from brazing to room temperature as a consequence of the thermal mismatch, the different elastic-plastic properties and the different phase transformation behavior of the components during the cooling cycle. In our first attempt to investigate the brazing-induced residual stresses in components of steel and cemented carbide, a simple sample geometry consisting of two quadratic plates of about equal thickness was considered (Bing *et al.*, 1996). Here, we report on a study considering a more complex geometry coming close to the geometry of a real tool, i.e. the head of a rock drill. Moreover, different steel types were used to explore the dependence of the residual stress state on the material properties of the steel body. As was done by Bing *et al.* (1994; 1996), we tackled the problem both experimentally by X-ray and neutron diffraction and theoretically by finite-element calculations.

## EXPERIMENTAL

### Sample Preparation

The geometry of the samples is illustrated in Fig. 1. It was chosen as to resemble the head of a rock drill. Three types of steel were used for the bodies, i.e. a plain carbon steel (German grade Ck 45), a low alloyed steel (42 CrMo 4) and an air-hardening tool steel (German grade 42 NiCrMo 16 6). Because our investigations of the samples made of the steel 42 CrMo 4 are still at a relatively early stage, this report is focused on results obtained for the other two steels. The cemented carbide plates used were commercially available cutting edges and consisted of 73% WC, 17% (Ti, Ta, Nb)C, and 10% Co. The 0.2 mm wide gap between the steel body and the cemented carbide plate was filled with a foil consisting of Cu as braze metal and a Ni mesh to keep the thickness of the brazing gap constant after melting of the Cu in the brazing process. This is important because the residual stress state of a brazed

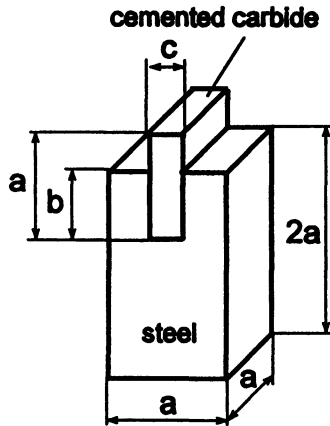


FIGURE 1 Geometry of the samples with  $a = 19$  mm,  $b = 13$  mm, and  $c = 5$  mm.

joint depends significantly on the thickness of the brazing gap. Brazing was done using hydrogen as reducing shielding gas. The samples were heated to  $1100^{\circ}\text{C}$  within about 20 min, kept at temperatures of  $1100\text{--}1180^{\circ}\text{C}$  for about 10 min, and then cooled down to room temperature within about 45 min. Due to this cooling cycle, the plain carbon steel resulted in a normalized state and the air-hardening steel in a martensitic state.

### Neutron Stress Analysis

The bulk of the neutron measurements were performed on the diffractometer G5.2 located at a cold neutron guide of the ORPHEE-reactor at Saclay. A neutron wavelength  $\lambda = 0.285$  nm yielded scattering angles  $2\theta \approx 90^{\circ}$  for the  $\{110\}$ -diffraction profile of steel and  $2\theta \approx 100^{\circ}$  for the  $\{101\}$ -diffraction profile of WC, which is the most intense of all WC-diffraction profiles in the neutron case. Since the strain data taken on the martensitic steel showed a very large scatter, additional measurements were carried out on this sample using the  $\{211\}$ -diffraction profiles. Such measurements require a shorter neutron wavelength and therefore were feasible only on a diffractometer located at a thermal beam tube. These measurements were carried out on the diffractometer 3T using a neutron wavelength of  $\lambda = 0.117$  nm. The gauge volume shaped by slits in the incident and the diffracted

beam was chosen such as to achieve a spatial resolution of 1 mm in the direction perpendicular to the interface between steel and cemented carbide, whereas the spatial resolution in one or both other directions was more relaxed (3–7 mm) to gain intensity.

In an attempt to optimize the diffractometer configuration comparative measurements were carried out using a position-sensitive detector (PSD) and a single detector with a large vertical acceptance as described by Pintschovius (1996). Illustrative results are shown in Fig. 2. For the sake of comparison, the total counting time was 30 min in all cases. The profiles (a)–(c) correspond to measurements of the {110}-reflection profile of the steel 42 CrMo 4 observed on the same sample with the same spatial resolution and at the same depth. It might seem surprising that the highest intensity was not obtained with the

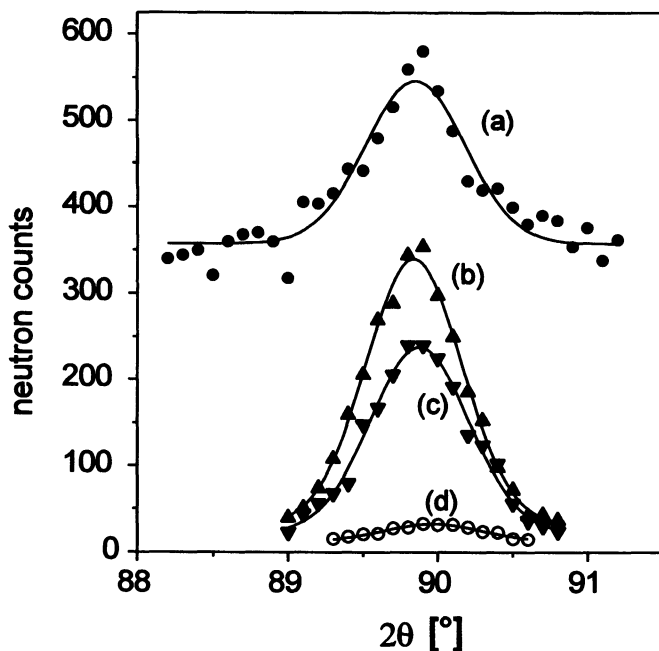


FIGURE 2 {110}-neutron diffraction profiles of the steel 42 CrMo 4 observed with a position-sensitive detector (a) or with a single detector with a large vertical acceptance and a 6 mm-detector slit (b) or a 4 mm-detector slit (c), respectively. Scan (d) shows a {101}-neutron diffraction profile of cemented carbide recorded with the same detector configuration as profile (c) and downshifted in  $2\theta$  by  $10^\circ$ . The counting time was 30 min for all four profiles.

PSD, but with the single detector and a detector slit width of 6 mm, however, this result is fully understandable by considering the much larger vertical acceptance of the single detector. Since the increase of the detector slit width from 4 to 6 mm did not significantly increase the observed linewidth – because of an inherent broadening of the reflection line – a further slight gain in measuring speed might have been obtained by further opening up the detector slit for this series of measurements. However, the superiority of the single detector was already evident not so much because of a slightly higher intensity, but because of the much lower background counting rate. In order to show how crucial it was to achieve a low background counting rate, a typical {101}-profile of WC is included into Fig. 2 as curve (d). For the sake of comparison, the number of counts of spectrum (d) have been divided by 6 in order to correspond to the same total counting time as the other spectra, i.e. 30 min. As a result of the test measurements, all subsequent measurements were performed using the single detector with a large vertical acceptance.

The lattice spacings were measured in three directions assumed to be the principal strain directions as inferred from the sample symmetry. For some areas of reduced local symmetry, additional measurements were carried out in intermediate directions. The values of the stress-free lattice spacings were determined from stress-free reference samples. Stress evaluation was done using the diffraction elastic constants  $s_1 = -\nu/E$  and  $\frac{1}{2}s_2 = (1 + \nu)/E$  with  $E = 210$  GPa and  $\nu = 0.28$  for the {110}- and the {211}-diffraction profiles of steel (Eigenmann and Macherlauch, 1996) and  $E = 658$  GPa and  $\nu = 0.19$  for the {101}-diffraction profile of cemented carbide according to Bing (1995). The measurements focussed on regions close to the interface between steel and cemented carbide where the calculations predicted the highest residual stress levels.

### X-RAY Stress Analysis

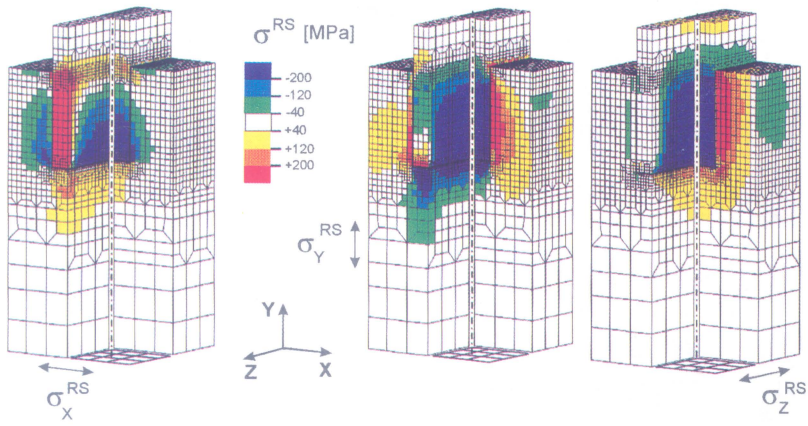
X-ray residual stress measurements on selected surface areas of the steel bodies were performed with a computerized  $\psi$ -diffractometer of the Karlsruhe type using {211}-diffraction profiles and V-filtered Cr  $K\alpha$ -radiation with a wavelength of  $\lambda = 0.22910$  nm. Stress evaluation was based on the  $\sin^2\psi$ -method employing the same diffraction elastic

constants as in the neutron case. In order to avoid effects of a possible slight surface oxidation or decarburization, surface layers of 50  $\mu\text{m}$  thickness were removed by electropolishing prior to the X-ray measurements. X-ray residual stress analyses on the surfaces of brazed cemented carbide plates did not yield reliable results since complex chemical reactions occur at the cemented carbide surfaces under the brazing conditions used. No method, neither chemical nor mechanical, could be found to remove these surface layers without modifying the residual stress states of the underlying layers.

### FINITE ELEMENT CALCULATIONS

The finite element calculations of the residual stress distributions were performed using the ABAQUS version 5.4 as solver, I-DEAS for pre-processing, and ABAQUS-POST for post-processing. As a consequence of the rather complex sample geometry, a realistic model had to be of 3 dimensions. The FE-mesh was refined towards the interfaces of cemented carbide, braze metal, and steel as shown in Fig. 3. For the cemented carbide, temperature independent linear elastic material behavior was assumed (Bing, 1995). The temperature dependent elastic-plastic material properties of the steels were given by Besserdich (1993) for the steel Ck 45 and by Böhler (1996) for the steel 42 NiCrMo 16 6. The temperature dependent thermal expansion coefficients of Cu are found in Gmelin (1955) and Landolt Börnstein (1964). The thermal expansion of the steels Ck 45 and 42 NiCrMo 16 6 and of the cemented carbide was investigated by dilatometer measurements. Results are shown in Fig. 4. Obviously, the cemented carbide exhibits the smallest thermal expansion and a practically linear behavior in the temperature range considered. The steels show a volume decrease associated with the  $\alpha$ - $\gamma$ -transformation during heating between about 730°C and 780°C. The corresponding volume expansion due to the  $\gamma$ - $\alpha$ -transformation during cooling occurs with a characteristic hysteresis between about 700°C and 650°C for the steel Ck 45 and between about 220°C and 80°C for the steel 42 NiCrMo 16 6. The ferritic-perlitic transformation of Ck 45 goes along with a much smaller volume expansion than the martensitic transformation of the steel 42 NiCrMo 16 6. The low transformation temperature is a

Ck 45



42NiCrMo16 6

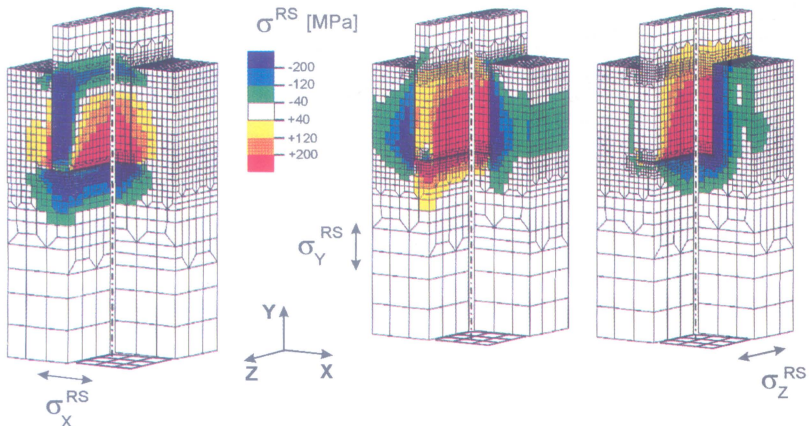


FIGURE 3 Three-dimensional-FE-mesh and calculated residual stresses in the x-direction (left), in the y-direction (middle) and in the z-direction (right) in brazed joints of a cemented carbide plate and a steel body of Ck 45 (top) and of 42 NiCrMo 16 6 (bottom). (See Color Plate I at the back of the issue.)

consequence of the alloying elements. The thermal expansion of the  $\gamma$ -phase is generally more pronounced than that of the  $\alpha$ -phase.

The braze metal consisting of Cu containing a Ni-mesh was, in a first step, modelled separately using temperature dependent elastic-plastic materials data of Cu and Ni. The material data for Ni are found in

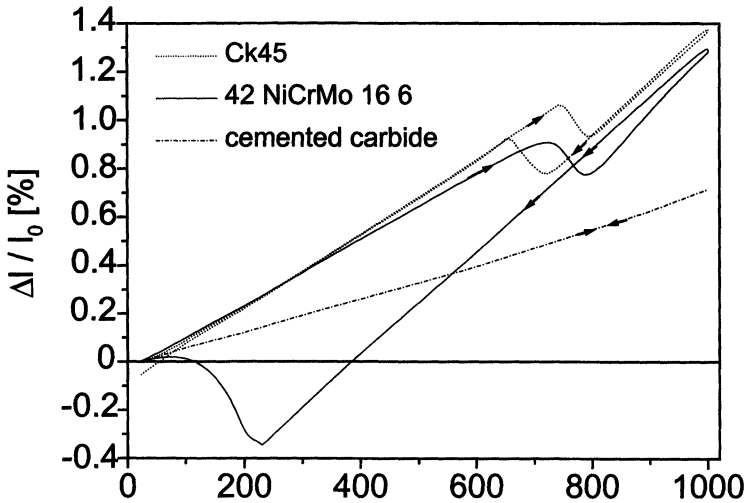


FIGURE 4 Dilatometer curves of the steels Ck 45 and 42 NiCrMo 16 6 and of cemented carbide, measured during heating and cooling between room temperature and 1000°C.

Gmelin (1967). The cooling cycle of the composite structure of the braze metal was simulated in a finite element model in order to obtain the residual stresses in the Cu-matrix and in the Ni-mesh. Subsequently, the elastic-plastic behavior of the composite braze metal was calculated taking into account the residual stresses in the structure. It turned out that, due to the influence of the residual stresses, the elastic-plastic properties of the composite braze metal are practically identical with those of Cu – at least for small plastic deformations. Therefore, the material data of Cu were used for further calculations.

## RESULTS AND DISCUSSION

The results of FE-residual stress calculations are given in Fig. 3 for the outer surfaces and the two center cross sections of the brazed joints of Ck 45 and cemented carbide (top) and 42 NiCrMo 16 6 and cemented carbide (bottom), respectively. The residual stress components  $\sigma_x^{RS}$ ,  $\sigma_y^{RS}$ , and  $\sigma_z^{RS}$  in the  $x$ -, the  $y$ -, and the  $z$ -direction are depicted in the left, middle, and right part of the figure, respectively. Generally, for both

types of samples, relatively high residual stress values are calculated only in the vicinity of the interface between steel and cemented carbide. They decrease rapidly with increasing distance from the interface. Further than about 5 mm away from the interface, only small residual stresses are calculated.

The residual stress development in the sample of Ck 45 and cemented carbide can be readily explained by the thermal expansion behavior of both materials (see Fig. 3). The volume expansion of the steel due to the  $\gamma$ - $\alpha$ -transformation occurs at high temperatures where the yield strengths of steel and braze metal are low which severely restricts the residual stress generation. Therefore, the residual stress development is dominated by the more pronounced thermal shrinkage of steel compared to that of the cemented carbide at temperatures below the transformation temperature of the steel. This thermal mismatch also leads to distortions of the samples which are schematically shown in the upper part of Fig. 5 for the indicated cross sections. Notwithstanding the fact that they result from a combination of thermal shrinkage and

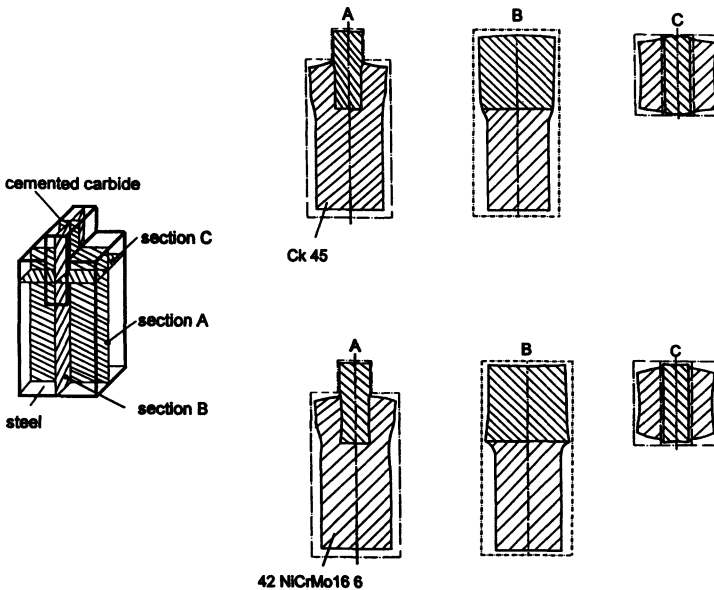


FIGURE 5 Scheme of distortion of the brazed joints of cemented carbide and Ck 45 (top) and 42 NiCrMo 16 6 (bottom) after cooling to room temperature.

elastic as well as plastic deformations, they can be used to understand the residual stress development. The hindered shrinkage of the steel in the  $x$ - and  $z$ -directions at the slot bottom leads to tensile residual stresses  $\sigma_x^{\text{RS}}$  and  $\sigma_z^{\text{RS}}$  in that region. They are compensated by compressive residual stresses in these directions in adjacent regions of the cemented carbide plate. The residual stress development in the  $y$ - and the  $z$ -direction in the steel on both sides of the cemented carbide plate and in the cemented carbide in between can be understood in a similar way. The compressive residual stresses in the steel on both sides of the cemented carbide plate in the  $x$ -direction are a consequence of the hindered shrinkage of the steel in this direction at the slot bottom.

It is found that failure critical concentrations of tensile residual stresses (red color in Fig. 3) in the brittle cemented carbide plate are predicted to occur in those surface areas which undergo local convex deformations (see distortion schemes in Fig. 5). As can be seen from cross section C in the upper part of the figure, this is the case for the side face of the cemented carbide plate which exhibits tensile residual stresses in the  $x$ -direction. In an analogous manner, the tensile residual stresses in the cemented carbide in the  $y$ -direction at the lower end of the side face and near the upper end of the steel body can be understood (see also cross sections B and A, respectively, in the upper part of Fig. 5). These locations correlate well with the starting point of cracks initiated by mechanical loading of the samples as described by Schrieck *et al.* (1997).

The residual stress state calculated for the samples with a steel body of 42 NiCrMo 16 6 is shown in the lower part of Fig. 3. The calculated residual stresses are of similar size but mostly of opposite sign when compared to those depicted in the upper part of Fig. 3. This can be explained by the volume expansion of the steel during the martensitic phase transformation at low temperatures which is evident from the respective dilatometer curve in Fig. 4. During cooling from brazing temperature, the larger thermal shrinkage of the steel body in comparison to that of the cemented carbide leads to a state of thermal, elastic, and plastic deformation which is qualitatively similar to that shown in the upper part of Fig. 5. The volume expansion of the steel associated with the martensitic phase transformation at the end of the cooling cycle finally changes that deformation state to the rather complex deformation state which is schematically sketched in the lower

part of Fig. 5. The volume expansion overcompensates the effects of the thermal mismatch at temperatures above the phase transformation which leads to an inversion of the sign of the residual stresses. This is the reason for the tensile residual stresses calculated in the  $x$ -, the  $y$ -, and the  $z$ -direction in the lower part of the cemented carbide plate. These tensile residual stresses caused failure of most of the samples during the cooling cycle at about  $70^{\circ}\text{C}$  by cracks in the cemented carbide plate.

In Fig. 6, some results of the FE-residual stress calculations are compared to results of X-ray residual stress analyses. It shows the residual stress component in the  $y$ -direction observed on the front side (upper diagrams) and on the side face along a line close to the interface to the cemented carbide plate (lower diagrams) as a function of the distance  $d$  from the top edge of the steel bodies. Evidently, the measured and calculated residual stress distributions agree rather well for the sample with the steel body of Ck 45. The scatter of the data by about  $\pm 12\text{ MPa}$  is larger than expected from the counting statistics,

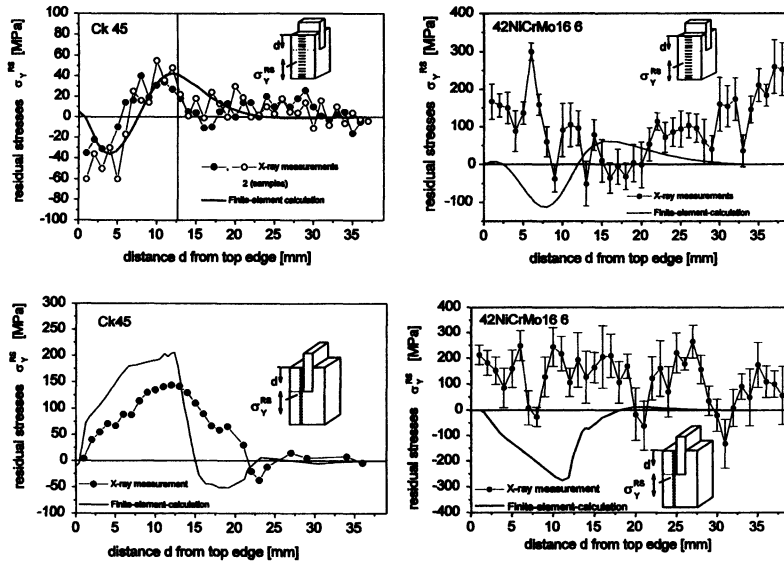


FIGURE 6 Residual stress distributions measured with X-rays (dots) and as calculated (full lines) along a line on the front surface (top) and on the side face (bottom) of brazed joints with a steel body of Ck 45 (left) and 42 NiCrMo 16 6 (right). Open and full dots refer to measurements on two different samples.

but is typical for measurements on ferritic–perlite steels and is generally assumed to be a consequence of different residual stress states of the  $\alpha$ -phase in the ferrite and in the perlite. Systematical discrepancies between measured and calculated residual stresses are found on the side face near the interface (lower diagram on the left-hand side). They are typical in that the FE-calculations tend to overestimate the measured residual stresses.

The diagrams on the right-hand side of Fig. 6 show that the surface residual stress distributions calculated for the samples with steel bodies of 42 NiCrMo 16 6 are not compatible with those measured by X-ray diffraction. In practically all areas investigated, the observed residual stresses were found to be tensile and reach values up to several 100 MPa. The large scatter of the data can only to a relatively small amount be attributed to the counting statistics of the severely broadened diffraction profiles of the martensitic steel. We think that the main reason is an inhomogeneous distribution of alloying elements on the scale of several 100  $\mu\text{m}$  which is typical for alloyed steels. This causes local variations of the stress-free lattice parameters as well as an inhomogeneous proceeding of the martensitic phase transformation which results in local variations of the residual stress states. Notwithstanding the large scatter of the measured data, the differences between measured and calculated residual stress distributions are significant. The reasons for these differences are not yet clear. Possibly, they are an effect of a slightly faster cooling of the surface which will cause the martensitic phase transformation to start at the surface and then proceed to the interior. This will, as it is known for such hardening processes, leave tensile residual stresses at the surface. Additional experiments will be needed in order to explore the thickness of the surface layers showing large tensile residual stresses.

Figure 7 (top) shows lattice strain distributions obtained by neutron diffraction in the interior of the steel bodies along the lines close to the interface which are indicated in the figure. In contrast to the data measured on the steel Ck 45 (left-hand side of Fig. 7), the data measured on the steel 42 NiCrMo 16 6 show a very large scatter similar to that observed and discussed above for the corresponding X-ray data. In order to improve the statistical reliability of the results, the evaluation included results for the  $\{110\}$ - as well as for the  $\{211\}$ -diffraction profiles. Moreover, lattice strain data were included into the evaluation

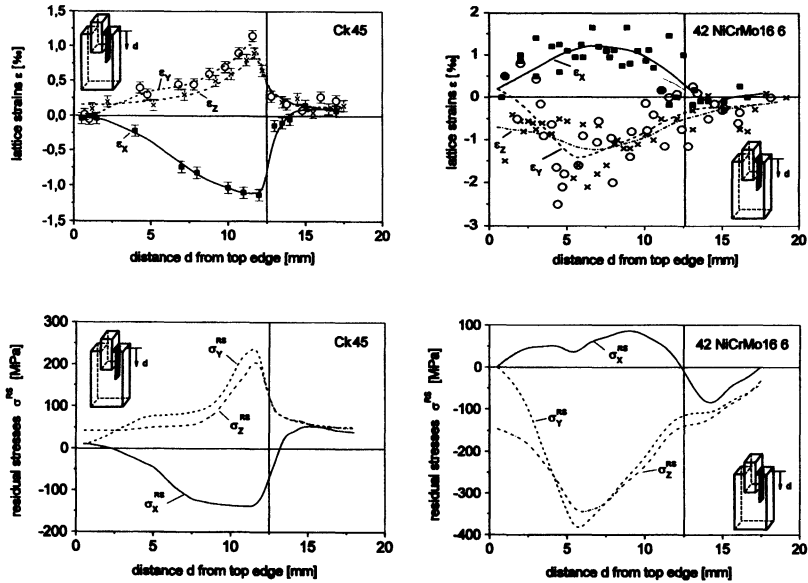


FIGURE 7 Top: lattice strain distributions in the principal strain directions measured by neutron diffraction (dots) along the indicated lines in the steel body close to the interface in brazed joints with steel bodies of Ck 45 (left) and of 42 NiCrMo 16 6 (right). The lines are spline functions fitted to the data. Bottom: residual stress distributions calculated from the spline functions shown in the diagrams above.

which were obtained in directions deviating  $\pm 5^\circ$  from the principal strain directions (corresponding to  $\Delta \sin^2 \psi < 0.01$ ). The residual stress distributions calculated from the measured lattice strain data are presented in the lower part of Fig. 7. The corresponding residual stress distributions in the cemented carbide plates are shown in Fig. 8. A comparison of the neutron diffraction results in Figs. 7 and 8 and the calculated residual stress distributions in Fig. 3 shows in general satisfactory agreement for both the samples with a steel body of Ck 45 and of 42 NiCrMo 16 6, respectively. Deviations between measured and calculated residual stresses, which are however not very large, occur for the residual stress components  $\sigma_y^{RS}$  and  $\sigma_z^{RS}$  in the Ck 45 where the values measured at distances  $d$  smaller than about 10 mm from the top edge of the steel body appear to be somewhat low. Since this tendency is not found in the corresponding residual stress distributions of the cemented carbide plate (see left diagram of Fig. 8), we assume that the investigated samples were, although prepared in an

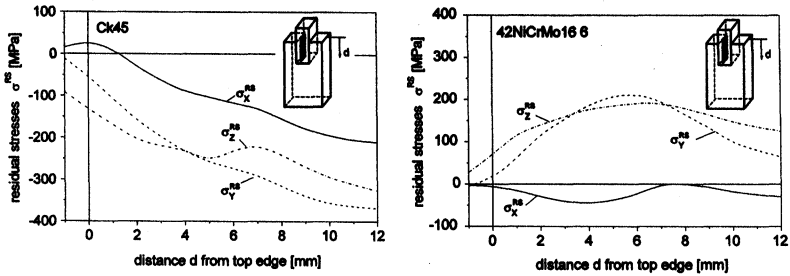


FIGURE 8 Residual stress distributions determined by neutron diffraction along the indicated lines close to the interface in the cemented carbide plates in brazed joints with steel bodies of Ck 45 (left) and 42 NiCrMo 16 6 (right). The residual stresses were calculated from spline curves fitted to strain data.

identical way, not really identical. This point will be investigated by further measurements.

The most significant difference between the results of neutron residual stress analyses and finite element residual stress calculations is found for the distribution of the residual stress component in the  $x$ -direction in the cemented carbide plate of the sample with the steel body of 42 NiCrMo 16 6. Whereas the calculation predicts relatively high tensile residual stresses in the lower part of the cemented carbide plate (i.e. close to the slot bottom), the measurements yielded small compressive values in that region which remains unexplained.

## CONCLUSIVE REMARKS

Though the residual stress distributions in brazed joints with steel bodies of Ck 45 or 42 NiCrMo 16 6 are very different, exhibiting a change of sign in many regions, failure critical concentrations of tensile residual stresses in the brittle cemented carbide occur in both types of joints. They can cause failure of the joints either on cooling from brazing temperature or due to subsequent cyclic loading. Indeed, a currently performed series of fatigue tests (Schrieck *et al.*, 1997) has shown that crack initiation starts at location of maximum tensile residual stresses in the cemented carbide. FE-calculations were performed in the hope to understand how the residual stresses develop and, in a next step, what should be done to reduce failure critical

concentrations of residual stresses. We have shown that the predicted residual stress distributions are in general in satisfactory agreement with those found in the bulk of the material, and so the FE-model comes largely up to our expectations. Further investigations will have to explore why the model tends to overestimate the residual stresses and why the residual stresses observed at the surface of martensitic steel bodies do not correlate with the predicted ones.

### *Acknowledgements*

The neutron scattering experiments were financially supported by the program 'Human Capital and Mobility – Access to Large Scale Facilities' of the European Community (Contract No. ERB CHGECT 920001). Substantial financial support of the presented research work by the Deutsche Forschungsgemeinschaft (DFG) is also gratefully acknowledged. The authors are also thankful to Dr. W. Weise and Mr. W. Malikowski, DEGUSSA AG Hanau, for valuable discussions and practical support in brazing the samples.

### *References*

- Besserdich, G. (1993). Eigenspannungs- und Verzugsausbildung beim Abschrecken von Zylindern aus den Stählen 42 CrMo 4 und Ck 45 unter Berücksichtigung der Umwandlungsplastizität. *Thesis*, Universität Karlsruhe (TH).
- Bing, K., Eigenmann, B., Scholtes, B. and Macherauch, E. (1994). Brazing residual stresses in components of different metallic materials. *Mat. Sci. Eng. A*, **174**, 95–101.
- Bing, K. (1995). Eigenspannungs- und Verzugsausbildung beim Hartlöten verschiedener metallischer Werkstoffe mit dem Edelstahl Ck 45. *Thesis*, Universität Karlsruhe (TH).
- Bing, K., Pintschovius, L., Eigenmann, B. and Macherauch, E. (1996). Combination of X-ray and neutron diffraction, hole drilling and FE-calculations for the determination of the residual stress state in brazed joints of steel and cemented carbide. *Proceedings of the fourth European Conference on Residual Stresses*, June 1996, Cluny, France (to appear).
- Böhler Edelstahl GmbH (1996). *Qualitätsinformationen*, A-8605 Kapfenberg/Austria.
- Eigenmann, B. and Macherauch, E. (1996). Röntgenographische Untersuchung von Spannungszuständen in Werkstoffen. *Mat.-Wiss. u. Werkstofftechnik*, part III: 27, pp. 426–437.
- Gmelins Handbuch der anorganischen Chemie* (1955). Kupfer Teil A. Leipzig: Verlag Chemie GmbH.
- Gmelins Handbuch der anorganischen Chemie* (1967). Nickel Teil 2, Leipzig: Verlag Chemie GmbH.
- Landolt Börnstein, Zahlenwerte und Funktionen* (1964). Band 4 Technik, 2. Teil Stoffwerte und Verhalten von metallischen Werkstoffen, Bandteil B.

- Pintschovius, L. (1996). Optimisation d'un diffractomètre pour la caractérisation des contraintes. In *Analyse des Contraintes Résiduelles par Diffraction des Rayons X et des Neutrons*, edited by A. Lodini and M. Perrin, pp. 129–136. Commissariat à L'énergie atomique.
- Schreieck, B., Eigenmann, B. and Löhe, D. (1997). Residual stresses and failure of brazed joints of cemented carbide and steel similar to cutting tools. In *Proc. of the 5th Int. Conf. on Joining of Ceramics, Glass and Metal, DVS-Berichte*, vol. 184, pp. 140–144. Düsseldorf: DVS-Verlag GmbH.